Babaryk, AA.; Contreras Almengor, OR.; Cabrero-Antonino, M.; Navalón Oltra, S.; García Gómez, H.; Horcajada, P. (2020). A Semiconducting Bi2O2(C4O4) Coordination Polymer Showing a Photoelectric Response. Inorganic Chemistry. 59(6):3406-3416. https://doi.org/10.1021/acs.inorgchem.9b03290

Semiconducting $Bi_2O_2(C_4O_4)$ Metal-Organic Framework showing Photoelectric Response

Artem A. Babaryk,[1] Oscar R. Contreras Almengor, [1] María Cabrero-Antonino,[2] Sergio Navalón,[2] Hermenegildo García,[2*] Patricia Horcajada[1*]

[1] *Advanced Porous Materials Unit, IMDEA Energy Institute. Av. Ramón de la Sagra 3, 28935 Móstoles-Madrid, Spain*

[2] *Departamento de Química and Instituto de Tecnología Química (CSIC-UPV), Universitat Politécnica de València, C/Camino de Vera, s/n, 46022 Valencia, Spain.*

Abstract. Owing to their efficient photoinduced electron/hole separation, inorganic semiconductors have been extensively considered as some of the most promising materials to convert solar light into electricity or chemical energy. Therefore, there is much interest on developing stable and photoactive materials. Bismuth oxides and, in particular, those built up of $[Bi_2O_2]^{2+}$ layers show an efficient charge separation and, thus, high photocatalytic activities. To explore possible synergetic effect of Bi metallic nodes and the electron-rich linker squarate, the $Bi_2O_2(C_4O_4)$ or IEF-3 (IMDEA Energy Framework) was hydrothermally prepared and fully characterized. As determined from X-ray structure, $[Bi_2O_2]^{2+}$ layers are interconnected by squarate ligand, having the Bi local environment a pronounced effect of $6s^2$ lone pair. IEF-3 shows a high thermal and chemical robustness under relevant industrial aggressive media. A large panel of physicochemical methods were applied to recognize IEF-3 as an UV-absorbing n-type semiconductor, showing a photocurrent response similar to α-Bi_2O_3, but offering further possibilities of tuning of to electrochemical properties by modification of the ligand. In such a manner, the well-known compositional and structural versatility of MOFs may be applied in a future for a fine tuning of covalently bonded semiconductor systems.

Comentado [PH1]: Cuidado ,seria iono-covalente probablemente

INTRODUCTION.

Production and storage of sustainable energy are some of the priority challenges of the XXIst century in the field of energy (1, 2). A promising alternative to produce green energy is the use of solar light for the generation of electricity or the production of solar fuels (3-5). Therefore, there is much interest on developing stable and active materials with sunlight response. Due to the occurrence of photoinduced electron/hole separation, inorganic semiconductors have been considered over the years as one of the most promising materials in this domain (6, 7).

In this line, bismuth oxides have got a high recognition in the field of ultra-violet (UV) and visible light photocatalysis (8). Bi_2O_3 exists as five different phases, namely α, β, γ, δ and ω with different crystal structure and physico-chemical properties (12). Interestingly, these Bi_2O_3 polymorphs exhibit visible light responses with bandgap values between 2.1 and 2.85 eV (13-15), attracting a considerable attention as semiconductors for photovoltaics, photocatalysis and optoelectronics (9-11).

Further, Bi*O*X (*X* = Cl, Br, I) and Bi_2XO_6 (*X* = W, Mo) families exhibit $[Bi_2O_2]^{2+}$ layers (Figure 1), which are believed to be the responsible for photocatalytic activity, owing to their efficient charge separation properties. Basically, cationic substructure corresponds to unique electronic properties, explained by valence bands appearing due to the Bi orbitals at more negative potentials than O 2p. The interlayer space is capable to accommodate the array of small *X* anions (X^- = HCOO, Cl, Br, I; X^{2-} = CO_3,

$BO_2(OH)$, $(OH)NO_3$, S, Se, Te) (16-22). By its modification, rich opportunities for bandgap engineering are opened, reaching the broad optical bandgap range of 1.8-3.4 eV, that matches to the desired photons energies of absorbed UV-visible part of the spectrum. The simplicity of preparation of such materials, using popular solvo(hydro)thermal synthesis at moderate temperatures (typically, 100–200 ºC), good yields and tunable particles size and morphologies, result in demonstrated capacities towards energy or environmental applications (16,19,20). It includes partial or full water photolysis into H_2 and O_2, and photodecomposition of small organic water contaminants (*e.g*. dyes or drugs).

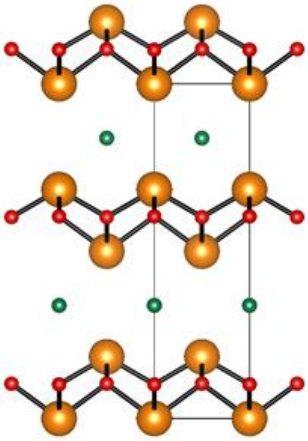

Figure 1. A projection of BiOCl shows representative $[Bi_2O_2]^{2+}$ layers with *X* = Cl atoms residing in interlayer space (bismuth, oxygen and chlorine atoms are depicted as orange, red and green spheres, respectively).

However, one of the limitations of inorganic semiconductors is the poor tunability of their structure to alter their physico-chemical properties to enhance visible light photoresponse (23). In this regard, the elementary Bi-O chromophore, present in bismuth oxides, can also be incorporated in other materials. In particular, metal organic frameworks (MOFs) are crystalline coordination polymers built-up from inorganic unit (*e.g.* atoms, clusters, chains, layers) and organic polydentate ligands (*e.g.* carboxylates, phosphonates, azolates), that could include Bi-O motives within their structure. In this context, MOFs enjoy from some of the properties of inorganic semiconductors, such as the occurrence of photoinduced charge separation, but with the advantage of a high chemical and structural versatility, offering a wide range of possibilities to tune their optical properties (24-26). Bismuth coordination polymers are known to be robust and possess prerequisites for photocatalytic-aided conversion of guest molecules (27-31).

Considering the above mentioned, the main objective of this work is to prove that larger *X* anions could be linked to $[Bi_2O_2]$ layers to fine-tune the optical properties of the resulting material, while retaining the desired cation substructure. Thus, as *X* anion, we have selected the squarate ligand, which is a highly conjugated system of C–C and C–O bonds in cyclobutene cycle with a compact rigid planar geometry. Its close linkage, guaranteed by short C_4O_4, eventuates in close proximities between metal centers, correlating to magnetic structuring (33) and zero thermal expansion (34, 35). Additionally, π-electron density is easily polarizable, which is valid for squarate.

Further, its average electronegativity (χ = 2.96, as defined by Allen (38)) is intermediate between soft X anions like $\chi(S)>\chi(Se)=2.55$ and hard $\chi(BO_2(OH))>\chi(Cl)>\chi(CO_3)>3.19$. In other words, one could anticipated that squarate will lift up the valence bands closer to conductance bands than any other reported inorganic oxo-ligand. From other side and despite their interesting properties, squarate has been scarcely used as ligand in MOFs. To the best of our knowledge, only three works report squarate-based MOFs (with Sn, Fe and Ca, respectively), (32, 36, 37) exhibiting interesting performances in separation processes and heterogeneous catalysts, with however no information about their optical properties.

Therefore, we report here the hydrothermal synthesis of the first Bi-squarate MOF (IEF-3; IEF for IMDEA Energy Framework), investigating not only its structural and spectroscopic features, but also its bonding and electronic organization together with its photocatalytic performances, using a combined experimental and computational approach. The photoelectrochemical characterization of IEF-3 showing the currents of charge separation opens the way the development the general strategy to find tune the photocatalytic properties of Bi_2O_3 to semiconductor by appropriate selection of the organic ligands.

MATERIALS AND METHODS

Synthesis of IEF-3 ($C_4O_6Bi_2$). A mixture of $Bi(NO_3)_3{\cdot}5H_2O$ (1.084 g, 2.23 mmol, Alfa Aesar, 98%), 3,4-dihydroxycyclobut-3-ene-1,2-dione (squaric acid, 0.765 g, 6.70 mmol, Across Organics, 99%) and deionized water (15.3 mL) was stirred in air for 15 min to afford uniform suspension. The mixture was transferred to a 23 mL Teflon-lined steel autoclave and heated up to 160ºC for 12 h, kept isothermally for 48 h and cooled down to 30 °C at a rate of 0.18 °C min^{-1}. The resulting pale-grey solid was filtered out, obtaining a yield of 49.2 % (0.6169 g) based on Bi source.

General Procedures. All chemicals were purchased from commercial sources and used as received without further purification. Attenuated total reflectance Fourier transformed infrared spectroscopy (ATR-FTIR) data were collected on a Nicolet 6700 instrument. Scanning electron microscopy (SEM) images toward the morphology studies were collected on a Hitachi TM-100 microscope at of 15 kV accelerating voltage. Energy dispersive X-ray analysis (EDX) was used to quantify bismuth content by Hitachi SwiftED-TM EDX system. Thermogravimetric analysis (TGA) and Differential scanning calorimetry (DSC) were carried out using a TA instruments SDT Q-600 simultaneous thermal analyzer under air or argon flow of (100 mL min^{-1}) with a heating rate of 5 °C min^{-1}. Raman spectrum was recorded in a range of 50–2000 cm^{-1} on a JASCO NRS-5100 spectrometer equipped with 532 nm laser source operating at 0.7 mW power. Solid state UV−vis absorption spectra were measured on a Perkin-Elmer Lambda 1050 UV/Vis/NIR spectrometer equipped with integrating sphere using $BaSO_4$ as reflectance reference. Elemental analysis was performed on bulk sample on a Thermo Scientific Flash 2000 simultaneous analyzer. The powder X-ray diffraction (PXRD) pattern of the final product was recorded at room temperature on a Malvern Panalytical Empyrean diffractometer, equipped with a PIXcel one-dimensional hybrid pixel technology position-sensitive device detector and operated

with Ni-filtered CuKα radiation (λ= 1.54178 Å). The sample was loaded in a Si-cut flat specimen sample holder and the data were collected in a range of 10-125° 2θ.

PXRD Structure Solution. The experimental pattern was indexed (M_{20} = 34) (39) to a monoclinic system, using peak positions in the region of 2θ = 14–59 by volume dichotomy algorithm, as implemented in DICVOL04 (40). The intensities of individual reflections were extracted by Le Bail fitting (R_p = 3.7%, R_{wp} = 5.1%) using the $P2_1/c$ group setting. Positions of Bi and O atoms were determined by direct methods (41). All asymmetric unit contents were localized by inspection of Fourier difference maps. The final solution was checked with Platon software (42) and *C*2/*m* space group was suggested by displacing C and O atoms. More symmetric model was engaged into re-refinements to yield Rp = 4.0%, Rwp = 5.2%, GoF = 1.92 residual factors, as established by Rietveld (43). No signs of structural distortions compatible with previous $P2_1/c$ space group were detected, therefore, the higher symmetry solution was used hereafter.

Cyclic voltammetry measurements were carried out using a standard three-electrode electrochemical cell using a fluoride-doped tin oxide (FTO)-coated glass substrate with IEF-3 as working electrode, a platinum wire as the counter electrode and a standard calomel electrode (SCE) as the reference electrode. IEF-3 was deposited on FTO-coated glass substrate by the doctor blade method using a suspension of IEF-3 (75 mg) in acetone (1 mL) and α-terpineol (0.5 mL). The employed electrolyte consisted of a dry acetonitrile solution of tetrabutylammonium hexafluorophosphate (0.1 M; $TBAPF_6$) solution. The solution was deaerated flushing Ar at least 15 min before the measurement.

Photocurrent experiments were performed using the same configuration and three-electrode and electrolyte solution as for cyclic voltammetry. Oxygen was removed from the cell by bubbling an Ar stream through the electrolyte. Irradiation was performed using an optical fiber connected to a 300 W Xe lamp. The photocurrent was measured under dark and upon illumination polarizing the working electrode at potentials from 1.6 to -0.2 V. Analogous experiments were performed adding to the electrolyte solution methanol (300 µL) or a 0.1 N aqueous solution of $Ce(NH_4)_2(NO_3)_6$ (10 µL).

Impedance spectroscopy measurements were carried out using also the standard three-electrode electrochemical cell. In these measurements, the working electrode consisted of a glassy carbon electrode supporting IEF-3. A drop of IEF-3 was deposited on the glassy carbon electrode from a mixture containing IEF-3(10 mg) in acetylacetone with Palaroid-b72 (9:1; total volume 0.2 mL) as a binder. The electrolyte consists of an acetonitrile solution of $TBAPF_6$ (0.1 M). Prior to the measurements, the electrolyte was purged by Ar to remove air. X-ray photoelectron spectra (XPS) were recorded on a SPECS spectrometer equipped with a MCD-9 detector using a monochromatic Al X-ray source.

Comentado [PH2]: definir

Computational Methods. Density functional theory (DFT) total energies and equilibrium geometries were plane-wave-based pseudopotential code ABINIT (44). The generalized gradient approximation (GGA) in Perdew-Burke-Ernzerhof parametrization, revised for solids and surfaces in combination with optimized norm-conserving Vanderbilt pseudopotentials, (45) were used. A convergence study revealed that a Monckhorst-Pack grid of 4×8×8 (40 k-points) sufficient for calculations

with respect to energies. The electronic (ionic) force was converged until 5×10^{-5} Ha/bohr $Å^{-1}$. The plane-wave cutoff for calculations was set to 40 Ha based on energy convergence tests. For a band structure calculation, the band path, that included all special k-vector points and lines, was generated using SeeK-path tool (46).

RESULTS AND DISCUSSION

Synthesis and characterization of IEF-3. IEF-3 was hydrothermally synthesized at 160 °C using 6-fold excess of squaric acid. It is known that, $Bi(NO_3)_3{\cdot}5H_2O$ hydrolyzes under acidic condition over 20-650 °C to basic salts, comprising $[Bi_6O_4(OH)_4]^{6+}$ and $\{[Bi_6O_5(OH)_3]^{5+}\}_2$ polynuclear cations (47). Under basic conditions (*e.g.*, addition of urea), $Bi_2O_2CO_3$ was detected as the final decomposition product. In contrast, here, in presence of the squaric acid, IEF-3 product was obtained at pH = 1.9 as microcrystalline powder with size distribution 40±10 μm (Figure 1a). The structure of IEF-3 was solved by direct methods from high resolution PXRD. Initially, $P2_1/c$ space group was assigned to the unit cell, allowing Bi, O and partially C placement from the electronic density. The rest of C atoms were located from series of difference Fourier map. Elemental analysis of IEF-3 is consistent (exp. C = 8.94(2)% wt., calc. = 8.55 % wt. from CHN analysis and calc. Bi = 76.9% wt., exp. = 74.3 % from EDX) with the framework structure determined from the PXRD data. Rietveld method refined model with stoichiometric formula unit was checked with Platon software (42) and *C*2/*m* symmetry setting was suggested (Figure 2). As figure-of-merit differed only

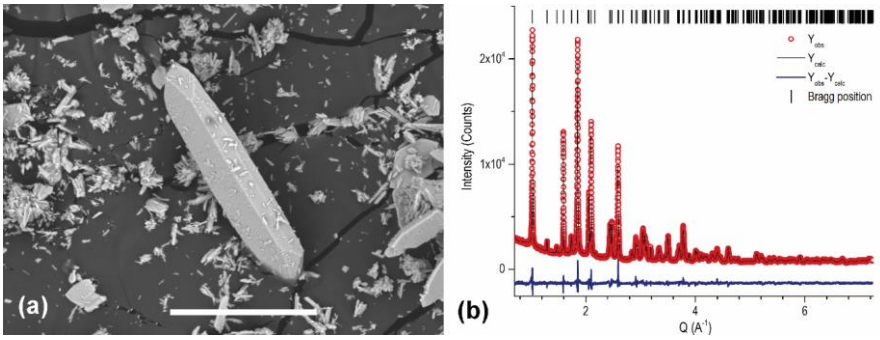

Figure 2. Left: Observed microcrystal morphology of IEF-3 solid (scale bar is equal to 30 μm). Right: Rietveld refined PXRD pattern of IEF-3 (final C2/*m* is adopted).

marginally for both refined models, the high symmetry solution was eventually adopted. As one can see from Figure 3, $[Bi_2O_2]^{2+}$ cations are organized in binodal (Bi and O) ribbons propagating along *c*-axis.

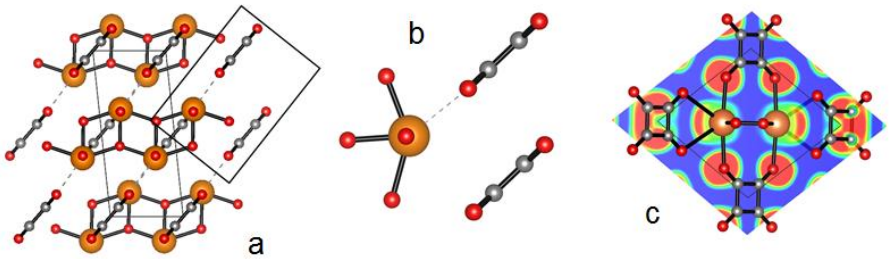

Figure 3. View of the IEF-3 structure projected onto (110) plane, the local coordination environment of Bi atom is highlighted with black lines (a), also given in enlarged form (b), the contacts larger than 2.7 Å are shown as dashed lines. An isosection of the calculated electron localization function surface (η = 0.65), showing Bi $6s^2$ electron lone pair (c).

Bi···Bi separation equals to 3.517(3) Å and Bi-O-Bi bond angle 107.0(7)°. Bond valence distances span over an 2.15(1)-2.22(2) Å interval. Neighbor Bi atoms are double-capped with squarate anions and apical oxygen atoms are distant from Bi centers by 2.418(8) Å. The anionic rigid moieties join to adjacent ribbons, engaging all four oxygen atoms, therefore, acting as μ_4-briding ligand. Additionally, lateral interaction of Bi atom and adjacent squarate residue is detected at a distance of 3.04934(5) Å. The complete metal environment (consisting of seven oxygens) is asymmetric, since all contacts are distributed within one hemi-sphere around the central atom. Typically, it may indicate the effect of $6s^2$ lone electron pair on the coordination polyhedron, which should be AB_7E (BiO_7E, in the particular case), as required by valence-shell electron-pair repulsion (VSEPR) theory. This detail is noticeable in view of correlation of Bi^{3+} $6s^2$ lone electron pair with electronic structure of photocatalysts. As previously mentioned, Pb^{2+} or Bi^{3+} 6s lone pair is engaged in valence bandgap engineering for the modification of the optical absorption without losses of photocatalytic activity (48). In other cases, unshared electron pair may also certainly impact on the photocatalytic activity. For instance, Wu *et al*. assumed that distorted BiO_7E coordination induces local dipoles, facilitating the charge separation process (49). Curiously, $Sn_2O(C_4O_4)(H_2O)$ geometry is affected by stereo-active lone pair of Sn^{2+},(50) while for $Pb(H_2O)(C_4O_4)$ the closest sphere of Pb^{2+} is

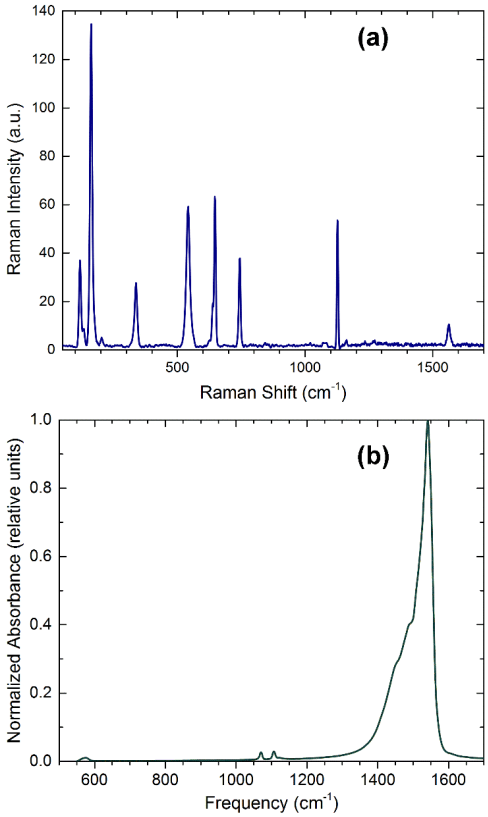

Figure 4. ATR-FTIR (top) and Raman (bottom) spectra of IEF-3.

Table 1. Summary of observed ATR-FTIR bands and Raman peaks assignment to vibrational modes of IEF-3.

$Bi_2O_2(C_4O_4)$		Tentative assignment
IR	Raman	
1559, 1540 1490, 1452	1561	B_{1g} ν(CO)
	1127	B_{2g} ν(CC)
	744	A_{1g} ring breathing
	647	E_g δ_{oop}(CO)
	638	B_{1g} ν(CC)
576	540	ν(Bi-O)
	336	δ(C=O)
	201 161 131 117	Lattice vibration modes

compactly filled with bridging water molecules and mono- and bidentately coordinated ligands (51).

Further insight into the structural details are revealed using FTIR and Raman spectroscopies (Figure 4). Typically, a bias of vibration mode registered with IR-spectroscopy is ~4 cm^{-1} ($5x10^{-4}$ eV), sufficiently small to follow changes in local geometries of molecular fragments. As determined by unit cell contents and the symmetry (52), $10A_g+8B_g$ Raman active modes are generally possible, and eleven of those are observed in the present study (Table 1). The most energetic characteristic combinational vibrational mode ν(C=C) + ν(C=O) is not observed from the present data. The band, centered at 1540 cm^{-1}, is responsible for B_{1g} ν(CO) vibration of squarate anion. Notably, it is red-shifted in accordance with E_g δ_{oop}(CO) by *ca*. 20 cm^{-1} with respect to the uncoordinated anion (53), that might indicate some covalent contribution to Bi–O(–C) bonding. Weak doublet at 1106 and 1070 cm^{-1} are mainly scissoring of ν(C=C) bonds. Broad peak at 540 cm^{-1} does not fall close into predicted or observed frequencies of C_4O_4 anion vibrations, but it matches for stretching of short Bi–O bonds, albeit in ν(Bi-O) was observed at 489 cm^{-1} for BiOI photocatalyst (54). Indeed, Bi-O interatomic distances in BiOI are longer (2.34 Å) (55), indicating a higher iconicity when compare with those determined for IEF-3 (2.15(8)-2.22(2) Å).

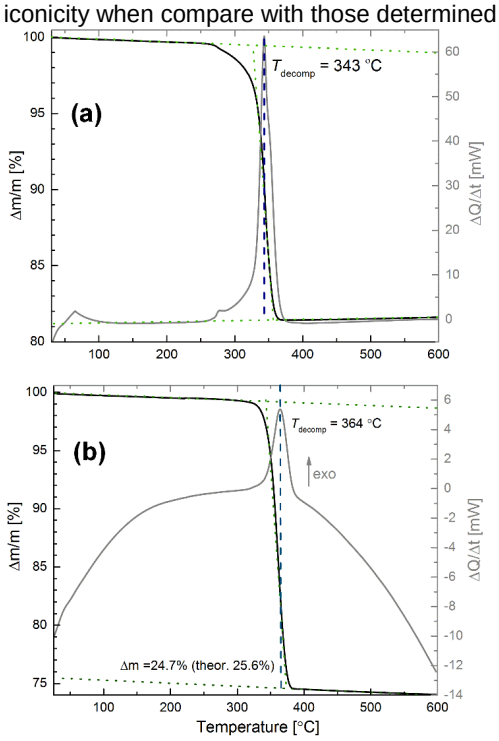

Figure 5. TGA-DSC traces of IEF-3 recorded at open air (left) and argon (right) atmospheres.

The thermal stability of IEF-3 was checked with TGA under argon and air atmospheres. Under oxidative environment, the material resists up to 265 °C and then,

Comentado [PH3]: No hay termodifraccion de este material???

collapses due to pyrolysis of the ligand (Figure 5a), while without oxidizer the auto-reduction process takes place at 364 °C (Figure 5b). One can propose the following equations for the degradation of IEF-3 either under inert atmosphere (Eqn. 1) or oxidant conditions (Eqn. 2):

$$2C_4O_6Bi_2 + 5O_2 = 2Bi_2O_3 + 8CO_2 \text{ (Eqn. 1)}$$
$$C_4O_6Bi_2 = 2Bi + 2CO_2 + 2CO \text{ (Eqn. 2)}$$

The latter results in the formation of spherical microparticles of metallic bismuth of size ~50 µm, as observed by SEM (Figure S1). To the best of our knowledge, this is the first example of self-reduction reported for squarate systems under inert atmosphere. This might be exploited in future as a route for preparation of metallic nano- or microparticles. Overall, thermal stability in oxidizing atmosphere is comparable to other bismuth-carboxylate MOFs that do not collapse until 400 °C (27).
The chemical stability of IEF-3 material was also assessed by suspending the solid in different media, mimicking industrially relevant aggressive working conditions. As it can be fetched from the comparison of powder patterns of pristine and treated powders (Figure 6a), IEF-3 remains intact under acidic (pH = 2.5) and basic (pH = 10.2) conditions, and protonic and aprotic organic solvents (Figure 6b), suggesting stability of operation in corrosive solutions. A few reference independent researches on Bi-containing arylcarboxylate MOFs show a similar chemical resistance to either a range of low pHs (30,56) or solvents (57), but combined studies have never been performed before. This exceptional chemical stability is probably associated first, with the dense character of the solid and the absence of unsaturated metal sites, limiting the degradation to the contact surface. Further, when referring to the bond valence sums (BVS) as a simple measure of bond strength in IEF-3, equatorial Bi–O2 and apical Bi-O1 are the strongest ones (0.41-0.86 valence units, v.u.), indicating a high degree of covalency and thus, a high stability.

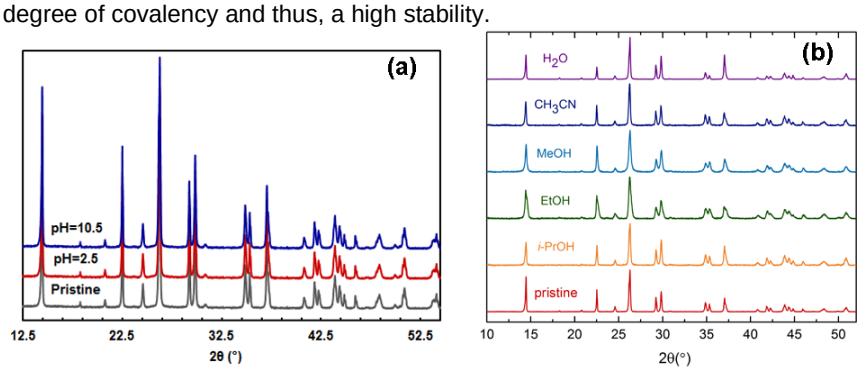

Figure 6. Stability tests on IEF-3 under acidic/basic conditions (a) and widely used chemical solvents (b).

As we mentioned above, there are many examples of inorganic solids based on $[Bi_2O_2]^{2+}$ fragments exhibiting photocatalytic properties. This motivated us to evaluated the optical properties of IEF-3. Thus, the optical bandgap was determined from the

Tauc plot on the Kubelka-Munk processed diffuse reflectance UV/vis data (Figure 6). IEF-3 exhibits an indirect type of transition, αhv ~(hv – E_g)$^{1/2}$, in agreement with our DFT calculations. The deduced optical bandgap (3.0 eV) is one of the smallest well amid reported for [Bi_2O_2]*X* materials (where *X* = BO_2(OH) (18), CO_3 (19) or (OH)NO_3 (20). This result supports well our initial hypothesis of a probable red-shifted optical absorption of bismuth squarate.

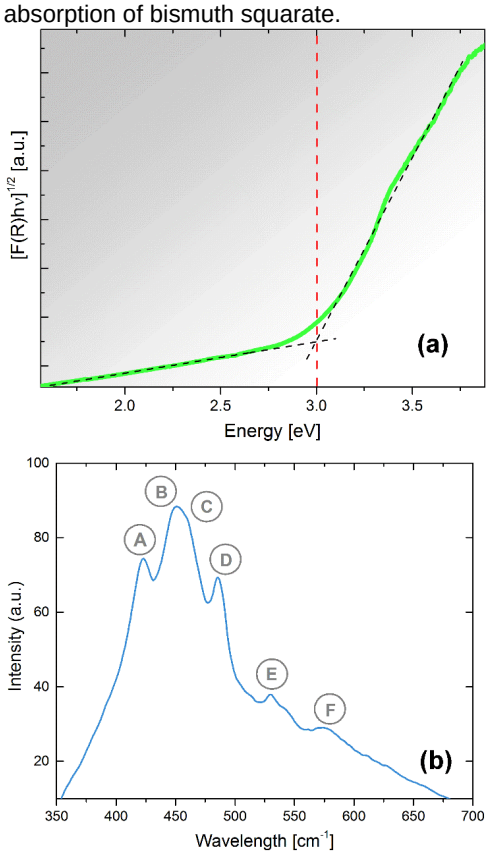

Figure 7. Left: Tauc plot of UV-vis diffuse reflectance spectrum analysis of IEF-3. Note: dashed lines are used as eyes guide-lines for the sake of clarity. Right: Solid state emission spectrum of IEF-3. Observed peaks are denoted with capital Latin letters.

The light emission properties were investigated with steady-state luminescence spectroscopy. Upon λ_{ex}=350 nm excitation, IEF-3 shows several emission lines (denoted as A-F; see Figure 7). A-band at 425 nm is close by energy to fundamental absorption. The B-F bands are likely attributed to squarate-ion transitions, as assigned previously (58).

Considering the structure of IEF-3 in where Bi^{3+} cations are also coordinated to oxygen, it was assumed that the photochemical behavior of IEF-3 could be somehow similar to that of bismuth oxides. The yellow powder α-bismuth oxide p-type

semiconductor with a bandgap of 2.85 eV (10) was used as reference. Thus, to gain information on the electrochemical properties of IEF-3, cyclic voltammetry was initially performed on the IEF-3 in degassed CH_3CN using $TBAPF_6$ as an inert electrolyte. In the first part of the voltammetry, polarization towards negative potentials allowed recording three reductions peaks (denoted as R_1, R_2 and R^3 in Figure 8) at potentials of -0.50, -0.84 and -1.11 eV, respectively. These reduction peaks appear to be reversible since the corresponding oxidation peaks were recorded when the bias potential was decreased. Observation of the corresponding anodic peaks associated to the reduction waves indicated the existence of reversible redox peaks in IEF-3 material. From these electrochemical data, an estimation of the reduction potential of the conduction band (CB) minimum of IEF-3 in equilibrium with an electrolyte solution corresponding to R_1 was estimated as -0.18 V. After correction, this value is in relatively good agreement with the periodic DFT calculation for the energy of the CB minimum. From this value and the optical bandgap energy (determined from the Tauc plot of the absorption spectrum of 3.0 Ev), the oxidation potential of the valence band (VB) maximum was estimated to 2.82 V.

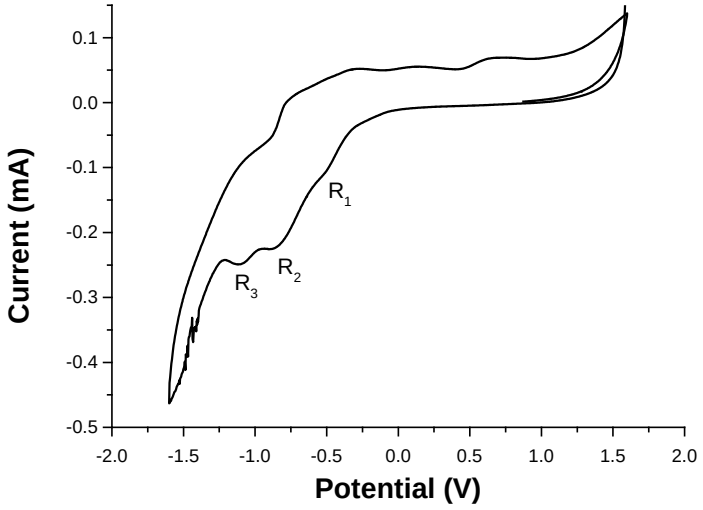

Figure 8. Cyclic voltammetry of IEF-3/FTO in deareated CH_3CN using $TBAPF_6$ as electrolyte. Scan was initiated towards negative potential. The three observed reduction waves have been labelled in the plot as R_i.

Comentado [PH4]: Mejorar calidd de imagen?

For an in-depth characterization of IEF-3, XPS was carried out (Figure 9). The expected C1s, O1s and Bi4f peaks were observed. In addition, an estimation of the valence band potential, based on the extrapolation of the first XPS peak of the spectrum after correction with the workfuncion of the instrument, gave a value for the VB) maximum about 2.99 eV. This experimental VB value based on XPS is in reasonable agreement with that one determined by cyclic voltammetry.

To put these CB and VB potential values into context, it should be mentioned that precedents in the literature have reported for α-Bi_2O_3 values of -0.07 and 2.69 eV,

respectively (59). Accordingly, characterization of IEF-3 indicates that this material has somewhat a larger bandgap, which is associated with an increase in the reduction potential of the CB minimum, as well as a slight increase in the oxidizing power of the VB maximum.

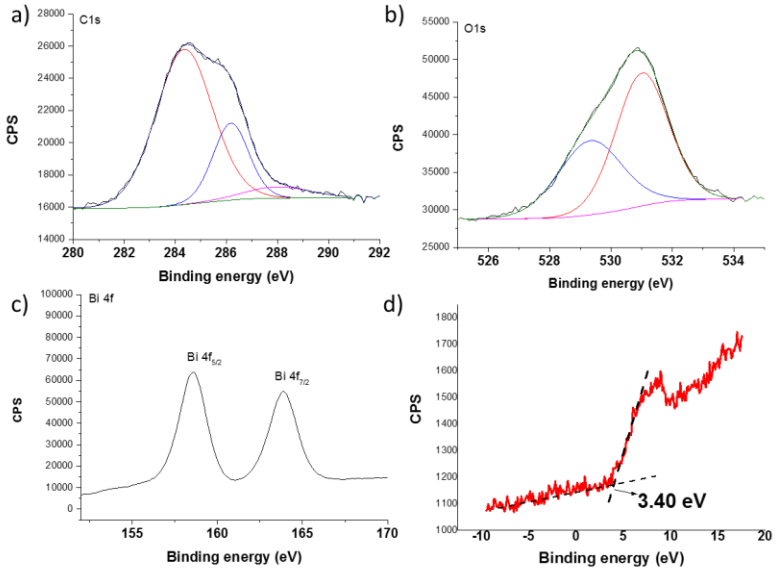

Figure 9. High resolution XPS peaks measured for IEF-3, corresponding to C1s (a), O1s (b), and Bi4f (c), as well as the onset part of the XP spectrum from where the VB potential was estimated.

One of the most convincing and safest ways to determine the photocatalytic behavior of a semiconductor is the observation of photocurrent upon illumination of electrodes of the material under different conditions. Aimed at establishing its semiconducting properties, photocurrent measurements of IEF-3 films were performed. IEF-3 films were prepared by the doctor blade method, depositing a suspension of the solid in α-terpineol onto a transparent conducting FTO electrode. Upon irradiation of IEF-3-FTO electrodes immersed into an acetonitrile solution of $TBAPF_6$ using Pt wire as counter electrode and Ag/AgCl as reference electrode, generation of photocurrent, whose intensity increased upon increasing the polarization voltage, was observed. Figure 10 illustrates the photocurrent response under different conditions.

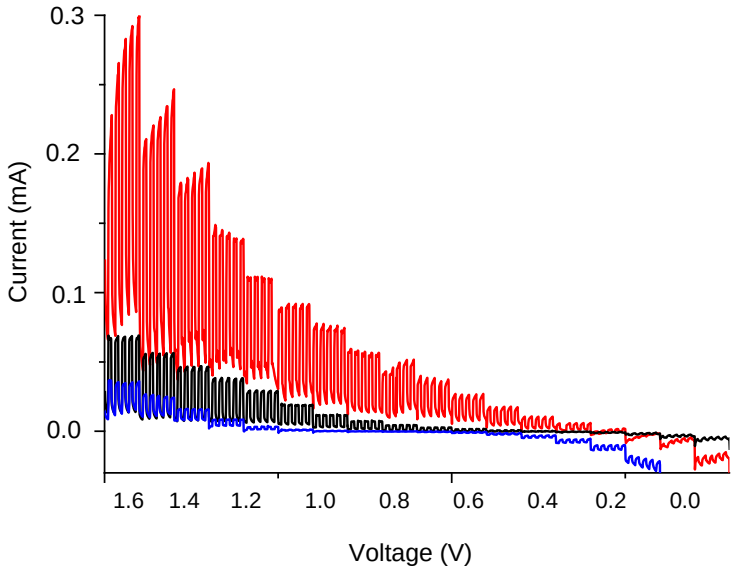

Figure 10. Photocurrent intensity *vs.* polarization potential measured for a IEF-3-FTO electrode in deaerated 0.1 M acetonitrile solution of $TBAPF_6$ in the absence of any additive (black line) or in the presence of MeOH (red line) or $Ce(NH_4)_2(NO_3)_6$ (blue line) upon illumination with the output of a 300 W Xe lamp.

Comentado [PH5]: Poner figura con mejor resolucion

As it can be seen in Figure 9, the current intensity shows a significant increase from 0.00843 to 0.06734 mA as the voltage increases from 0 to 1.6 V upon illumination of the IEF-3/FTO electrode with the output of a 300 W UV-vis Xe lamp. The intensity of the photocurrent decreases with the polarization voltage applied to the photoelectrode, changing from positive to negative at a voltage of about 0.45 V. This voltage corresponds to the onset potential to extract electrons from the IEF-3 semiconductor. It was observed that the photoresponse of the electrode depends on the presence of electron donor or acceptor compounds in the electrolyte. Thus, upon addition of methanol, both the dark current and the photocurrents increase considerably by a factor of 4.3, reaching a photocurrent intensity of 0.3 mA at 1.6 V. This behavior indicates that in the presence of methanol, IEF-3 acts as photocatalyst (see Scheme 1). Thus, in the presence of the well-known hole quencher methanol, photocurrent increases as consequence of the ability of this sacrificial agent to donate electrons, quenching holes generated after photon absorption and occurrence of photoinduced electron/hole separation. Due to the fast hole quenching by electrons provided by methanol, higher photocurrent intensity is reached.

It can also be seen in Figure 10 that for high photoresponses, appearance of a capacitive effect on the IEF-3 film is observed and, then, the photoresponse increases somewhat upon consecutive cycling due to the build-up of charges on the IEF-3 layer. This capacitative effect is observed for voltage values above 1.3 V and becomes much less important for lower polarization voltages.

As expected for a semiconductor undergoing charge separation upon photon absorption of energy higher than the bandgap, the presence of electron acceptors results in much smaller photoresponse (Figure 10). Thus, opposite to the effect of methanol, if Ce(IV) is present in the electrolyte solution, both dark current as well as photoresponse become considerably decreased as consequence of the scavenging of electrons upon irradiation of IEF-3 in the presence of Ce (IV), resulting in a much lesser number of electrons available for the photocurrent (Scheme 1).

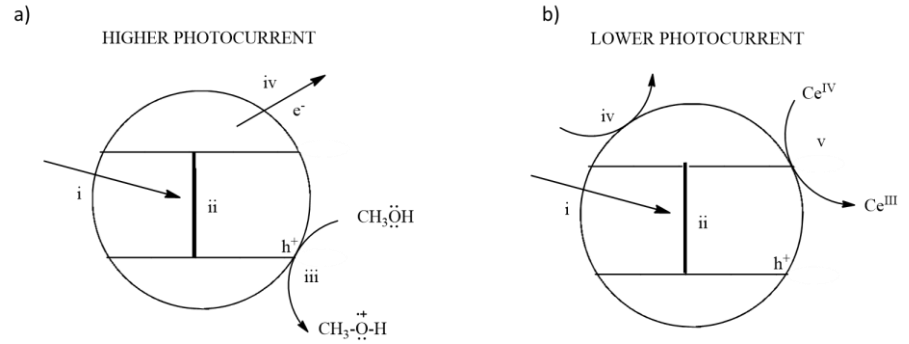

Scheme 1. Characteristic behavior of IEF-3 as semiconductor, as determined by the observation of photocurrent, whose intensity increases in the presence of methanol (a) and decreases in the presence of $Ce(NH_4)_2(NO_3)_6$ (b). i) Light absorption, ii) photoinduced charge separation, iii) hole quenching, iv) photocurrent, and v) electron quenching.

Further electrochemical characterization of IEF-3 films was performed by measuring impedance spectroscopy in the range of frequency from 900,000 to 5 Hz. The Nyquist plot of the experimental results allowed to determine the interfacial and internal resistance of the IEF-3 film by fitting the experimental data to a model with two parallel resistances and capacitances (see Figure S2 and S3). The results were compared with those of an analogous film of α-Bi_2O_3. Supporting information provides also the values corresponding to the electrolyte-solid interface resistance and the internal resistance for these two IEF-3/FTO and α-Bi_2O_3/FTO films, determined by the best fitting of the experimental data to the model. Based on these values, one can conclude that both IEF-3 and α-Bi_2O_3 materials exhibit similar impedance for the interfacial solid-electrolyte charge transfer, while the internal resistance and capacitance were significantly improved for the IEF-3 film compared to the Bi_2O_3 one.

Comentado [PH6]: Completar con el numero de la figura del supporting

Therefore, available photocatalytic characterization indicates that IEF-3 exhibits an analogous behavior as α-Bi_2O_3 semiconductor, with somewhat larger bandgap and reduction and oxidation potentials. IEF-3 undergoes charge separation upon irradiation in the UV range, photogenerated electrons and holes being able to participate into reduction and oxidation processes, respectively.

Further, electronic band structure was calculated using periodic boundary DFT calculations with the goal to correlate electronic fundamental bandgap with experimentally observed optical absorption onset value. As one can see from the diagram A(0, 0, 1/2) and Y2(-1/2,1/2,0), points of the first Brillouin zone represent the VB

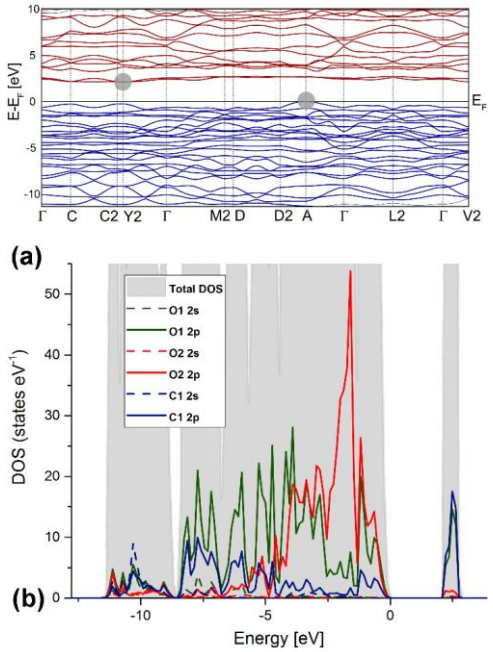

Figure 10. Left: Calculated energy band structure diagram of IEF-3. Valence and conductance bands are shown in solid blue and red colored lines, respectively. Right: The density of states plot of IEF-3.

zone maximum and CB zone minimum, respectively. The calculated electronic bandgap is 2.11 eV. This suggests that IEF-3 behaves as an indirect bandgap semiconductor. Generally, photon-electron interaction for indirect bandgap semiconductors decreases light absorption efficiency, therefore, a penetration depth is higher and thicker layer of photocatalyst is required for device fabrication (8). IEF-3 follows the trend along with other Bi_2O_2X having indirect type of main optical transition (17, 18, 20).

As frequently (60), this value is slightly smaller, but comparable, than the experimentally obtained, due to the existence of a derivative discontinuity of the energy with respect to the number of electrons. Further analysis of bonding trends when referring to the atom and orbital-resolved density of states pattern. Bi 6s, 6p orbitals are involved in hybridization with O2 2p states at the region E-E_F = -2.1…-1.3 eV. This fact is corroborated by the observed short bond distances d(Bi–O2) = 2.15 Å, d(Bi–O2^i) = 2.22 Å (*i*: -x, -y, -z), indicating strong interactions and leading to lower energy of molecular orbitals. The fact of almost equal contribution states from oxygen and carbon of the squarate ligand is obviously due to the high conjugation of aromatic orbitals. Surprisingly, the topmost valence bands are populated with non-bonding orbitals of bridging oxygen atoms and π-density of the squarate anion. The low-energy conductance states are almost exclusively represented by anti-bonding states of the squarate anions with some admixture of anti-bonding O2 and O1 2p states. For Bi*OX* (*X* = Cl, Br, I) (61) or Bi_2O_2Y (Y = S, Se, Te, NCN) (21, 22, 62) compounds featuring $[Bi_2O_2]^{2+}$, Bi 6s states are strongly overlapped with O 2p and *X* atom p-states, yielding

Comentado [PH7]: Falta verbo???
No se entiende

VBs. Due to this feature, bandgap engineering is admitted in a broad range from 3.4 eV (BiOCl) to 1.8 eV (Bi_2O_2NCN). Further, due to the delocalized nature of conjugated pi-electron density, squarate anions act rather similar to anions with low electronegativity uplifting VBs to E_F.

From the other side, CBs of reference $[Bi_2O_2]^{2+}$ layered materials are almost exclusively composed of dominant empty Bi 2p orbitals with some contribution of O 2p states. This is not the case for IEF-3, where anti-bonding states determine the composition of CBs, similarly to organic molecular materials (63).

From other point of view, squarate species act supplying shallow states, modulating $[Bi_2O_2]^{2+}$ electronic structure. This fact might be a reason to revise our ideas for designing new bismuth-based semiconducting materials for energy or environmental applications.

CONCLUSIONS

In this work, we have successfully combined the rigid geometry of aromatic squarate ($C_4O_4^{2-}$) with the characteristic topology of $[Bi_2O_2]^{2+}$ to yield the called IEF-3 metal-organic framework. Bismuth coordination environment is unambiguously affected by the $6s^2$ lone pair, as experimentally determined and computationally corroborated, in agreement with classic VSEPR theory. The reduction properties of the squarate ligand were revealed for the first time. IEF-3 exhibits a high thermal stability and exceptional chemical robustness in industrially relevant aggressive media. Its interesting light absorption and emission properties suggested the active role of squarate species, correlating with computed bulk electronic structure. Overall, photo-electrochemical behavior of IEF-3 was similar to α-Bi_2O_3, an ultraviolet light absorbing n-type semiconductor. Further, photocurrent measurements in the absence or presence of quenchers for IEF-3 films provided a firm evidence of the semiconductor behavior of IEF-3. The electron-enrichment of IEF-3 might be reasoned by electron-donating function of squarate anions. This fact has a major impact on the tunability of molecular semiconductor properties, opening interesting avenues for photochemical applications. In particular $[Bi_2O_2]^{2+}$ to semiconductors could be designed and modify using different substitutes and even other related organic ligands.

REFERENCES

(1) Lund, H. Renewable Energy Strategies for Sustainable Development, *Energy* **2007**, *32*, 912-919.

(2) Omer, A.M. Energy, environment and sustainable development, *Renew*. *Sustain*. *Energy Rev*. **2008**, *12*, 2265-2300.

(3) Crabtree, G.W.; Lewis, N.S.; Solar Energy Conversion, *Phys*. *Today* 2007, 60, 37-42.

(4) Fahrenbruch, A.; Bube, R. Fundamentals of Solar Cells: Photovoltaic Solar Energy conversion, Elsevier, 2012.

(5) Gust, D.; Moore, T.A.; Moore, A.L. Solar Fuels Via Artificial Photosynthesis, *Acc*. *Chem*. *Res*. **2009**, *42*, 1890-1898.

(6) Arakawa, H.; Sayama, K. Oxide Semiconductor Materials for Solar Light Energy Utilization, *Res*. *Chem*. *Intermed*. **2000**, *26*, 145-152.
(7) Sang, Y.; Liu, H.; Umar, A. Photocatalysis from UV/Vis to Near-Infrared Light: Towards Full Solar-Light Spectrum Activity, *ChemCatChem* **2015**, *7* 559-573.
(8) Wang, Q.; Domen, K. Particulate Photocatalysts for Light-Driven Water Splitting: Mechanisms, Challenges, and Design Strategies. *Chem*. *Rev*. **2019**, https://doi.org/10.1021/acs.chemrev.9b00201
(9) Liu, Z.; Yan, F. The Application of Bismuth-Based Oxides in Organic-Inorganic Hybrid Photovoltaic Devices, *J*. *Amer*. *Ceram*. Soc. **2012**. *95*, 1944-1948.
(10) Raza, W.; Haque, M.; Muneer, M.; Harada, T.; Matsumura, M. Synthesis, Characterization and Photocatalytic Performance of Visible Light Induced Bismuth Oxide Nanoparticle, *J*. *Alloys* Compd. **2015**, *648*, 641-650.
(11) Gomez, C.L.; Depablos-Rivera, O.; Silva-Bermudez, P.; Muhl, S.; Zeinert, A.; Lejeune, M.; Charvet, S.; Barroy, P.; Camps, E.; Rodil, S.E. Opto-Electronic Properties of Bismuth Oxide Films Presenting Different Crystallographic Phases, Thin Solid Films **2015**, *578*, 103-112.
(12) Medernach, J.W.; Snyder, R.L. Powder Diffraction Patterns and Structures of The Bismuth Oxides, *J*. *Am*. *Ceram*. *Soc*., **1978**, *61*, 494-497.
(13) Leontie, L.; Caraman, M.; Alexe, M.; Harnagea, C. Structural and Optical Characteristics of Bismuth Oxide Thin Films, *Surf*. *Sci*. **2002**, *507*, 480-485.
(14) Xiao, X.; Liu, C.; Hu, R.; Zuo, X.; Nan, J.; Li, L.; Wang, L. Oxygen-Rich Bismuth Oxyhalides: Generalized One-Pot Synthesis, Band Structures and Visible-Light Photocatalytic Properties, *J*. *Mater*. *Chem*., **2012**, *22*, 22840-22843.
(15) Weidong, H.; Wei, Q.; Xiaohong, W.; Xianbo, D.; Long, C.; Zhaohua, J. The Photocatalytic Properties of Bismuth Oxide Films Prepared Through the Sol–Gel Method, *Thin Solid Films*, **2007**, *515*, 5362-5365.
(16) Duan, F.; Zheng, Y.; Liu, L.; Chen, M.; Xie, Y. Synthesis and Photocatalytic Behaviour of 3D Flowerlike Bismuth Oxide Formate Architectures. *Mater. Lett.* **2010**, *64*, 1566-1569.
(17) Lee, G.-J.; Zheng, Y.-C.; Wu, J.J. Fabrication of Hierarchical Bismuth Oxyhalides (BiOX, X = Cl, Br, I) Materials and Application of Photocatalytic Hydrogen Production from Water Splitting. *Catal. Today.* **2018**, *307*, 197−204.
(18) Huang, H.; He, Y.; Lin, Z.; Kang, L.; Zhang, Y. J. Two Novel Bi-Based Borate Photocatalysts: Crystal Structure, Electronic Structure, Photoelectrochemical Properties, and Photocatalytic Activity under Simulated Solar Light Irradiation. *Phys*. *Chem*. *C*, **2013**, *117*, 22986-22994.
(19) Liu, Y; Wang, Z.; Huang, B.; Yang, K.; Zhang, X.; Qin, X.; Dai, Y. Preparation, Electronic Structure, and Photocatalytic properties of $Bi_2O_2CO_3$ Nanosheet. *Appl*. *Surf*. *Sci*., **2010**, *257*, 172-175.
(20) Huang, H., He, Y.; Li, X.; Li, M.; Zeng, C.; Dong, F.; Du, X. $Bi_2O_2(OH)(NO_3)$ as a Desirable $[Bi_2O_2]^{2+}$ Layered Photocatalyst: Strong Intrinsic Polarity, Rational Band Structure and {001} Active Facets Co-Beneficial for Robust Photooxidation Capability *J*. *Mater*. *Chem*. *A*, 2015, 3, 24547–24556
(21) Ruleova, P.; Drasar, C.; Lostak, P.; Li, C. P.; Ballikaya, S.; Uher, C. Thermoelectric properties of Bi_2O_2Se. *Mater*. *Chem*. *Phys*. **2010**,*119*, 299−302.
(22) Luu, S. D. N.; Vaqueiro, P. Synthesis, characterisation and thermoelectric properties of the oxytelluride Bi_2O_2Te. *J*. *Solid State Chem*. **2015**, *226*, 219−223

(23) Yu, X.; Marks, T.J.; Facchetti, A. Metal Oxides for Optoelectronic Applications, *Nat*. *Mater*. **2016**, *15*, 383-396.
(24) Alvaro, M.; Carbonell, E.; Ferrer, B.; Llabrés F.X.; Xamena, I.; Garcia, H. Semiconductor Behavior of a Metal-Organic Framework (MOF). *Chem*. *Eur*. *J*. **2007**, *13*, 5106-5112.
(25) Usman, M.; Mendiratta, S.; Lu, K.L.; Semiconductor Metal–Organic Frameworks: Future Low-Bandgap Materials, *Adv*. *Mater*. **2017**, *29*, 1605071.
(26) Tachikawa, T.; Choi, J.R.; Fujitsuka, M. ; Majima, T. Photoinduced Charge-Transfer Processes on MOF-5 Nanoparticles: Elucidating Differences Between Metal-Organic Frameworks and Semiconductor Metal Oxides. *J*. *Phys*. *Chem*. *C* **2008**, *112*, 14090-14101.
(27) Feyand, M.; Mugnaioli, E.; Vermoortele, F.; Bueken, B.; Dieterich, J. M.; Reimer, T.; Kolb, U.; de Vos, D.; Stock, N. Automated Diffraction Tomography for the Structure Elucidation of Twinned, Sub-micrometer Crystals of a Highly Porous, Catalytically Active Bismuth Metal-Organic Framework. *Angew. Chem. Int. Ed.* **2012**, *51*, 10373-10376.
(28) Wang, G.; Sun, Q.; Liu, Y.; Huang, B.; Dai, Y.; Zhang, X.; Qin, X. A Bismuth-Based Metal-Organic Framework as an Efficient Visible-Light-Driven Photocatalyst, *Chem. Eur. J.*, **2015**, 21, 2364-2367.
(29) Wang, G.; Liu, Y.; Huang, B.; Qin, X.; Zhang, X.; Dai, Y.; A Novel Metal-Organic Framework Based on Bismuth and Trimesic Acid: Synthesis, Structure and Properties, *Dalton Trans*., **2015**, *44*, 16238-16241.
(30) Wang, Y.; Takki, S.; Cheung, O.; Xu, H.; Wan, W.; Ohrstrom, L.; Inge, A. K.; Elucidation of the Elusive Structure and Formula of the Active Pharmaceutical Ingredient Bismuth Subgallate by Continuous Rotation Electron Diffraction, *Chem*. *Commun*., 2017, 53, 7018-7021.
(31) Koeppen, M.; Dhakshinamoorthy, A.; Inge, A. K.; Cheung, O.; Angstrom, J.; Mayer, P.; Stock, N. Synthesis, Transformation, Catalysis, and Gas Sorption Investigations on the Bismuth Metal-Organic Framework CAU-17, *Eur*. *J*. *Inorg*. *Chem*. **2018**, *2018*, 3496-3503.
(32) Gándara, F.; Gómez-Lor, B.; Iglesias, M.; Snejko, N.; Gutiérrez-Puebla, E.; Monge. A. A New Scandium Metal Organic Framework Built Up From Octadecasil Zeolitic Cages as Heterogeneous Catalyst. *Chem. Commun.* **2009**, 2393-2395.
(33) Goswami, S.; Adhikary, A.; Jena, H.S.; Biswas, S.; Konar, S. A 3D Iron(II)-Based MOF with Squashed Cuboctahedral Nanoscopic Cages Showing Spin-Canted Long-Range Antiferromagnetic Ordering. *Inorg. Chem.* **2013**, *52*, 12064–12069.
(34) Usov, P.M.; Keene, T.D.; D'Alessandro, D.M. A Comparative Study of the Structural, Optical, and Electrochemical Properties of Squarate-Based Coordination Frameworks. *Aust. J. Chem.* **2013**, *66*, 429–435.
(35) Liu, Z.; Lin, K.; Ren, Y.; Kato, K.; Cao, Y.; Deng, J.; Chen, J.; Xing, X. Inorganic–organic hybridization induced uniaxial zero thermal expansion in MC_4O_4 (M = Ba, Pb). *Chem*. *Commun*. **2019**, *55*, 4107–4110.
(36) Goswami, S.; Jena, S.H.; Konar, S. Study of Heterogeneous Catalysis by Iron-Squarate based 3D Metal Organic Framework for the Transformation of Tetrazines to Oxadiazole derivatives. *Inorg*. *Chem*. **2014**, *53*, 7071−7073.
(37) Lin, R.-B.; Li, L.; Zhou, H.-L.; Wu, H.; He, C.; Li, S.; Krishna, R.; Li, J.; Zhou, W.; Chen, B. Molecular Sieving of Ethylene from Ethane Using A Rigid Metal–Organic Framework. *Nat*. *Mat.* **2018**, *17*, 1128–1133.

(38) Allen, L.C. Electronegativity is the average one-electron energy of the valence-shell electrons in ground-state free atoms. *J*. *Am*. *Chem*. *Soc*. **1989**, *111*, 9003–9014.
(39) Boultif, A.; Louer, D. Powder Pattern Indexing With The Dichotomy Method. *J*. *Appl*. *Cryst*. **2004**, *37*, 724–731.
(40) de Wolf, P.M. A Simplified Criterion For The Reliability Of A Powder Pattern Indexing. *J*. *Appl*. *Cryst*. **1968**. *1*, 108–113.
(41) Altomare, A.; Cuocci, C.; Giacovazzo, C.; Moliterni, A.; Rizzi, R.; Corriero, N.; Falcicchio, A. "EXPO2013: a kit of tools for phasing crystal structures from powder data", *J*. *Appl*. *Cryst*. **2013**, *46*, 1231–1235.
(42) Spek, A.L. Structure Validation In Chemical Crystallography. *Acta Cryst*. *D* **2009**, *65*, 148–155.
(43) Rietveld, H.M. A Profile Refinement Method For Nuclear And Magnetic Structures". *J*. *Appl*. *Cryst*. **1969**, *2,* 65–71.
(44) Gonze, X.; Amadon, B.; Anglade, P.M.; Beuken, J.-M.; Bottin, F.; Boulanger, P.; Bruneval, F.; Caliste, D.; Caracas, R. ; Cote, M.; Deutsch, T.; Genovese, L.; Ghosez, Ph.; Giantomassi, M.; Goedecker, S.; Hamann, D.; Hermet, P.; Jollet, F.; Jomard, G.; Leroux, S; Mancini, M.; Mazevet, S.; Oliveira, M.J.T.; Onida, G.; Pouillon, Y.; Rangel, T.; Rignanese, G.-M.; Sangalli, D.; Shaltaf, R.; Torrent, M.; Verstraete, M.J.; Zerah, G.; Zwanziger, J.W. ABINIT: First-principles Approach to Material and Nanosystem Properties. *Comput*. *Phys*. *Commun*., **2009**, *180*, 2582–2615.
(45) Hamann, D.R. Optimized Norm-conserving Vanderbilt Pseudopotentials. *Phys*. *Rev*. *B*, **2013**, *88*, 085117
(46) Hinuma, Y.; Pizzi, G.; Kumagai, Y.; Oba, F.; Tanaka, I. Band structure Diagram Paths Based On Crystallography. *Comp*. *Mat*. *Sci*. **2017**, *128*, 140-184.
(47) Christensen, A. N.; Jensen, T. R.; Scarlett, N. V. Y.; Madsen, I. C.; Hansond, J. C.; Altomare, A. In-situ X-ray powder diffraction studies of hydrothermal and thermal decomposition reactions of basic bismuth(iii) nitrates in the temperature range 20–650 °C. *Dalton Trans*., 2003, 3278-3282.
(48) Suzuki, H. H.; Kunioku, H.; Higashi, M.; Tomita, O.; Kato, D.; Kageyama, H.; Abe R. Lead Bismuth Oxyhalides $PbBiO_2X$ (X = Cl, Br) as Visible-Light-Responsive Photocatalysts for Water Oxidation: Role of Lone-Pair Electrons in Valence Band Engineering. *Chem*. *Mater*. **2018**, *30*, 5862−5869.
(49) Wu, X.; Li, M.; Li, J.; Zhang, G.; Yin, S. A Sillenite-Type $Bi_{12}MnO20$ photocatalyst: UV, Visible and Infrared Lights Responsive Photocatalytic Properties Induced by the Hybridization of Mn 3d and O 2p Orbitals. *Appl*. *Catal*., *B* **2017**, *219*, 132–141.
(50) Millet, P.; Sabadié, L.; Galy, J.; Trombe, J.C. Hydrothermal synthesis and structure of the first tin(II) squarate $Sn_2O(C_4O_4)(H_2O)$–comparison with $Sn_2[Sn_2O_2F_4]$. *J*. *Solid State Chem*., **2003**, *173*, 49-53.
(51) Bataille, T.; Bouhali, A.; Kouvatas, C.; Trifa, C.; Audebrand, N.; Boudaren, C. Hydrates and polymorphs of lead squarate $Pb(C_4O_4)$: Structural Transformations Studied by In Situ X-ray Powder Diffraction And Solid State NMR. *Polyhedron*, **2019**, 164, 123–131.
(52) Kroumova, E.; Aroyo, M.I.; Perez-Mato, J.M.; Kirov, A.; Capillas, C.; Ivantchev, S.; Wondratschek, H. Bilbao Crystallographic Server : Useful Databases and Tools for Phase-Transition Studies. *Phase Transitions* **2003**, *76*, 155–170.

(53) Junqueira, G.M.A.; Rocha, W.R.; De Almeida, W.B.; Dos Santos, H.F. Theoretical Analysis Of The Oxocarbons: The Solvent And Counter-Ion. *Phys*. *Chem*. *Chem*. *Phys*. **2003**, *5*, 437–445.

(54) Cao, J.; Xu, B.; Lin, H.; Luo, B.; Chen, S. Novel Heterostructured Bi_2S_3/BiOI Photocatalyst: Facile Preparation, Characterization and Visible Light Photocatalytic Performance. *Dalton Trans*. **2012,** *41*, 11482-11490

(55) Keller, E.; Kramer, V. A Strong Deviation from Vegard's Rule: X-ray Powder Investigations of the Three Quasi-Binary Phase Systems BiOX-BiOY (X, Y=Cl, Br, I) *Z*. *Naturforsch*., *B*: *J*. *Chem*. *Sci*. **2005**, *60*, 1255-1263.

(56) Gao, X.; Zhao, H.; Zhao, X.; Li, Z.; Gao, Z.; Wang, Y.; Huang, H. Aqueous Phase Sensing of Bismuth Ion Using Fluorescent Metal-Organic Framework. *Sens*. *Actuators*, *B* **2018**, *266*, 323-328.

(57) Deibert, B.J.; Velasco, E.; Liu, W.; Teat, S.J.; Lustig, W.P.; Li, J. High-Performance Blue-Excitable Yellow Phosphor Obtained from an Activated Solvochromic Bismuth-Fluorophore Metal–Organic Framework. *Cryst. Growth Des.* **2016**, *16*, 4178-4182.

(58) De Mello Donegá, C.; Ribeiro, S.J.L.; Gonçalves, R.R.; Blasse, G. Luminescence And Non-Radiative Processes In Lanthanide Squarate Hydrates. *J*. *Phys*. *Chem*. *Solids*, **1996**, *57*, 1727–1734

(59) He, R.; Zhou, J.; Fu, H.; Zhang, S.; Jiang, C. Room-Temperature In Situ Fabrication of Bi_2O_3/g-C_3N_4 Direct Z-scheme Photocatalyst With Enhanced Photocatalytic Activity. *Appl*. *Surf*. *Sci*. **2018**, *430*, 273–282.

(60) Mori-Sanchez, P.; Cohen, A.J.; Yang., W., Localization and Delocalization Errors in Density Functional Theory and Implications for Band-Gap Prediction. *Phys*. *Rev*. *Lett*., 2008, 100, 146401.

(61) Zhang, K.-L.; Liu, C.-M.; Huang, F.-Q.; Zheng, C.; Wang, W.-D. Study of the electronic structure and photocatalytic activity of the BiOCl photocatalyst. Appl. Catal., B 2006, 68, 125–129.

(62) Corkett, A.J.; Chen, Z.; Bogdanovski, D.; Slabon, A.; Dronskowski, R. *Inorg*. *Chem*. **2019**. *58*, 6467–6473

(63) Kohler, A.; Bassler, H. Electronic Processes in Organic Semiconductors. An Introduction; Wiley-VCH Verlag: Weinheim, 2015.